Geophysical Research Letters®

Key Points:

- The 2013 Mw 7.7 earthquake caused widespread aseismic slip along the megathrust
- Moment released by aseismic slip along megathrust corresponds to an Mw 7.3 earthquake
- Eastern Makran megathrust fault is locked to at most 220 km distance from the trench but not along the entire seismogenic width

Supporting Information:

Supporting Information may be found in the online version of this article.

Correspondence to:

Y. Shao,
shaoyun@radi.ac.cn

Widespread Aseismic Slip Along the Makran Megathrust Triggered by the 2013 Mw 7.7 Balochistan Earthquake

Xiaoran Lv[1,2] ⓘ**, Falk Amelung[3]** ⓘ**, and Yun Shao[1,2,4]** ⓘ

[1]Aerospace Information Research Institute, Chinese Academy of Sciences, Beijing, China, [2]University of Chinese Academy of Sciences, Beijing, China, [3]Rosenstiel School of Marine and Atmospheric Sciences, University of Miami, Miami, FL, USA, [4]Laboratory of Target Microwave Properties (LAMP), Zhongke Academy of Satellite Application in Deqing (DASA), Deqing, China

Abstract InSAR time series data for the 2014–2021 period reveal up to 20 cm of radar line-of-sight displacements in the area of the 2013 Mw 7.7 Balochistan earthquake northwest of the Hoshab Fault in the eastern Makran subduction zone in southwest Pakistan. We show that surface displacements were caused by ~80 cm of aseismic slip along a 5,500-km²-wide subhorizontal patch of the megathrust fault. The corresponding moment is Mw 7.3. The percentage of slip in plate-perpendicular direction ranges from ~65% in the northwest to 96% in the southeast. Slip is consistent with shear stress imparted by the 2013 earthquake. The triggered aseismic slip suggests that this section of the megathrust is decoupled. The implication for the seismic potential of the subduction zone is that the megathrust is fully locked to at most 220 km distance from the trench, consistent with the lack of M ≥ 9 earthquakes in the historic record.

Plain Language Summary The 2013 Mw 7.7 Balochistan earthquake was one of the worldwide largest earthquakes that occurred in the upper plate of a subduction zone within an accretionary prism. Using 2014–2021 InSAR data, we explore the post-seismic deformation mechanism. We find that post-seismic deformation is caused by widespread aseismic slip along the megathrust, induced by the static stress change imparted by the Balochistan earthquake. The detection of aseismic slip has implications for the seismic potential of the megathrust.

1. Introduction

The Makran subduction zone, where the Arabian oceanic plate thrusts under Eurasia, has one of the worldwide shallowest dipping subducting slabs (3–4° in Eastern Makran). According to thermal models, the down-dip limit of the seismogenic zone occurs at ~35 km depth, corresponding to a distance of 280 km measured from the trench (Khaledzadeh & Ghods, 2021). The earthquake potential remains enigmatic: Can the megathrust rupture along the entire seismogenic width, possibly generating a M8.8 earthquake as suggested by a geodetic plate coupling study (Frohling & Szeliga, 2016)? The contemporaneous seismicity of the Eastern Makran subduction zone is relatively low (Mokhtari et al., 2019), with the largest instrumentally recorded earthquake being the 1945 Mw 8.1 (Byrne et al., 1992), of which the tsunami killed ~4,000 or more people (Lohdi et al., 2021). Momeni et al. (2020) conclude that most coseismic slip occurred in the shallow part of the megathrust to a distance of 100 km from the trench. Megathrust earthquakes also occurred in 1483, 1756, and 1851 (Mokhtari et al., 2019) but there are no reports that these events were exceptionally large. Throughout this paper we refer with megathrust to the contact area between two plates which may involve one or multiple shear zones and which is not necessarily a single surface (e.g., Bilek & Lay, 2018).

The 24 September 2013 Mw 7.7 Balochistan earthquake, an upper-plate subduction zone earthquake in the eastern Makran provides an opportunity to study the response of the megathrust to stress field perturbations, and to probe the rheological behavior of the accretionary prism. It was largely a left-lateral strike-slip earthquake (strike-slip to dip-slip ratio of 6:1), rupturing 200 km of the arcuate, moderately dipping Hoshab Fault (50–70° towards northwest) with coseismic surface offsets of up to 15 m (Avouac et al., 2014; Jolivet et al., 2014; Vallage et al., 2015). Most of the slip was shallower than 15 km depth but the rupture reached 23 km in places. The earthquake occurred in the mature section of the accretionary prism along a fault unfavorably oriented to relieve stresses from subduction loading. Possible explanations are that the Hoshab Fault responds to both,
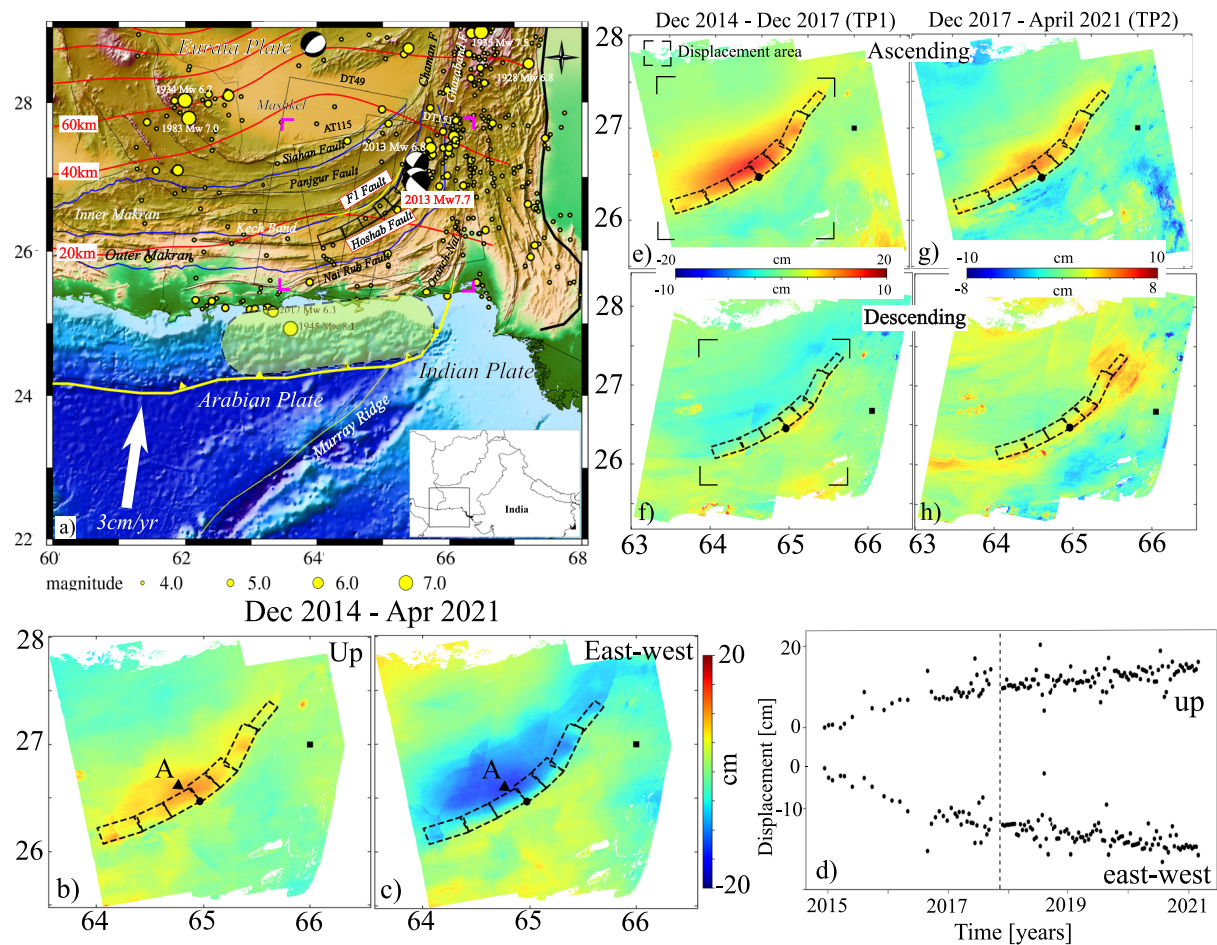
Figure 1. (a) Map of the study area with Sentinel-1 SAR coverage. Magenta corners: location of up and east-west deformation. Black solid rectangles: coseismic fault from Avouac et al. (2014). Yellow line: F1 fault. Yellow circles: 1928–2021 earthquakes from United States Geological Survey earthquake. Thick red lines: slab depth contours from the Slab2 model (Gavin et al., 2018). Yellow dashed rectangle: rupture zone of the 1945 earthquake. Cumulative (b) up and (c) east-west displacement components and (d) time series for a point located in the epicentral area. (e–h) Ascending and descending line-of-sight displacements for time periods 1 and 2. Black solid square in b–h: reference point: 27°N, 66°E for ascending, up and east-west; 26.6°N, 66°E for descending data. Black dashed rectangle in b–h: coseismic fault. Black dot: upper edge of the fault. Black triangle: point shown in (d). Black corners: area for modeling.

the Arabia-Eurasia subduction and the India-Eurasia transcurrent plate motion (Avouac et al., 2014; Barnhart et al., 2014; Penney et al., 2017).

2. Geologic Background

The subduction of the Arabian plate beneath Eurasia initiated in the late Cretaceous (Burg, 2018) then the Makran accretionary prism started to form. The contemporaneous convergence rate is ~3 cm/yr (Le Pichon & Kreemer, 2010). The prism is bounded by the Chaman-Ornach-Nal fault system, Minab-Sabzevaran fault system (located west of the area shown in Figure 1a), Gulf of Oman and the Mashkel depression (forearc basin) in the east, west, south and north, respectively. The along-strike and across-strike distances (from the deformation front in the Gulf of Oman to the Balochistan volcanic arc) are 1,000 km and 400–600 km, respectively (Jolivet et al., 2014). In the eastern Makran, the slab dips 3°–4° up to 210 km from the trench (the plate boundary or trench axis with sediments removed) where it increases to 9° (Motaghi et al., 2020; Smith et al., 2013). The depth of the slab is ~26 km beneath the Hoshab Fault and 40–50 km beneath the Mashkel depression (Figure 1a) (Gavin et al., 2018). The onshore prism has a very gentle surface slope (~1°). The small total taper of 4°–5° (Smith et al., 2012) suggests low friction (0.01–0.03) along the megathrust according to the Coulomb wedge theory (e.g., Penney et al., 2017). The main faults in eastern Makran are the Nai Rub, Hoshab and Panjgur faults (Figure 1a).

Within the Chaman fault system further north, the largest instrumental earthquake was the 1935 Mw 7.5 Quetta earthquake (Fattahi et al., 2015).

The Makran subduction zone has one of the worldwide thickest trench sediment layers (∼7 km thick). These water-rich sediments are scraped off from the down-going oceanic slab and accreted to approximately the same amounts by frontal and basal accretion (Burg, 2018; Platt et al., 1985). Therefore, the accretionary prism is characterized by high pore-fluid pressures varying with depth (Ruh, 2017). The megathrust fault has been located offshore at ∼8–10 km depth b.s.l. (Kopp et al., 2000; Smith et al., 2012) and under the Kech band at >12 km depth (Ellouz-Zimmermann et al., 2007).

A geothermal gradient of 20°C/km at the Kech Band indicates a relatively cool environment (Khan & Raza, 1986) of the prism. GPS-measured shortening of 6–8 mm/yr across the outer Makran likely reflects elastic strain to be released (Penney et al., 2017).

3. Data Analysis and Results

We used December 2014 to April 2021 Sentinel-1 SAR data from ascending track 115 and descending tracks 151 and 49 (154, 145, 150 acquisitions, respectively; two sub-swaths each track), and the Interferometric synthetic aperture radar Scientific Computing Environment stack processor (Fattahi et al., 2017; Rosen et al., 2012) to create for each acquisition 4 nearest-neighbor interferograms with 38 and 14 looks in range and azimuth directions, respectively. For time series processing, we use the Miami InSAR time series software in Python (MintPy) (Yunjun et al., 2019). We corrected for phase contributions due to tropospheric delays using the ECMWF's ERA5 global atmospheric model, and for the solid earth tides. Given that seasonal tropospheric delay variations in Balochistan can reach 30 cm (Fattahi & Amelung, 2015), we demonstrate in the supplement that the ERA5 model efficiently removes the topography-related tropospheric delays from the InSAR signal (see Figures S1.1 and S1.2 in Supporting Information S1). We concatenate adjacent tracks (geocoded at 0.002° posting) by adding a constant that minimizes the median of the difference in the overlapping areas and then average the displacements (Fattahi & Amelung, 2016). Finally we combine the ascending and descending data to vertical and east-west displacement components, assuming that the ascending images are acquired the same day as the descending images although they were acquired 4 days later. Throughout this paper we display the ascending data with linear ramps removed because of ionospheric contributions (see Figure S2.1 in Supporting Information S1).

The data show lobes of up to 15 cm of up and west displacements in the area north of the rupture (Figures 1b and 1c), respectively. As the time series for a point near the rupture shows logarithmic trends (Figure 1d), we consider two distinct time periods: one year after the earthquake (December 2014) to December 2017 (time period 1), and December 2017 to April 2021 (time period 2). The data show up to 15 and 8 cm displacement towards the satellite (line-of-sight increase, yellow-red colors), respectively (Figures 1e–1h).

4. Modeling Approach

To explain the observed post-seismic displacements we consider models with viscoelastic relaxation, afterslip, and aseismic slip along secondary faults.

4.1. Viscoelastic Relaxation Models

A viscoelastic lower layer is sandwiched between the elastic upper layer and the elastic subducted slab. We can consider horizontal layers because of the small dip angle (slightly more than 4° northwest of the Hoshab Fault). The thickness of the accretionary prism is 26 km (sum of the thicknesses of the upper and of the lower prism). The free model parameters are the thickness of the upper prism and the viscosity of the lower prism. We consider linear Maxwell rheology and power law rheology with powers of 2 and 3.5 and use the RELAX software (Barbot & Fialko, 2010a, 2010b).

4.2. Aseismic Slip Models

We consider three types of models, each consisting of seven uniform elastic dislocations with geometries based on the coseismic slip model of Avouac et al. (2014). In the first model, afterslip occurs only along the down-dip

extensions of the coseismic fault segments (down-dip extension model). The second model entails aseismic slip along a secondary fault located north of the coseismic fault (the F1 fault, Zhou et al., 2015) without afterslip (secondary fault model). The secondary fault consists of three segments along the mapped surface trace. In the third model there is aseismic slip along a near-horizontal decollement fault as well as afterslip along the coseismic fault segments. The decollement fault is modeled by seven dislocations with variable width. We consider two decollement geometries. In one model the decollement is located near the base of the accretionary prism at 26 km depth (basal decollement model). In the other model the decollement is located within the prism at 15 km depth (mid-prism decollement model).

In the down-dip extension model we invert for the width, depth of upper edge, rake and slip of each dislocation (28 model parameters, Table S2.1 in Supporting Information S1), in the secondary fault model for the depth of the upper edge, width, rake and slip of the seven dislocations while length, strike and dip are fixed according to the coseismic model geometry and the surface trace for the F1 fault (40 parameters, Table S2.2 in Supporting Information S1). In the decollement models we invert for the width, dip, rake and slip of the decollement fault segments and for the rake and magnitude of afterslip of the seven coseismic dislocations (42 model parameters, Table S2.3 in Supporting Information S1). We use a layered half-space with the depths and properties (*p*-wave velocity, *s*-wave velocity, density, Qp and Qs) obtained from the CRUST1.0 database (Gabi et al., 2013). The Greens functions are calculated using the PSGRN/PSCMP software (Wang et al., 2006).

4.3. Inversion Approach

We sample from the data using the quadtree downsampling method and calculate the misfit function defined as:

$$\chi^2 = (\boldsymbol{d}_{obs} - \boldsymbol{d}_{sim})^T \boldsymbol{C}^{-1} (\boldsymbol{d}_{obs} - \boldsymbol{d}_{sim}) \tag{1}$$

where $\boldsymbol{d}_{obs}$ and $\boldsymbol{d}_{sim}$ are observed and simulated displacements, respectively, and C is the covariance matrix, calculated using the semivariogram method to characterize the errors in InSAR data (Bagnardi & Hooper, 2018). $\boldsymbol{d}_{obs}$ contains 310, 352, 252 observations for time period 1 and 456, 482, 300 observations for time period 2 from ascending track 115 and descending tracks 151 and 49, respectively. The data are sampled from each of the three swaths without any concatenation that is, without averaging the data in overlap areas. For each of the three swaths we invert for linear ramps (constant offset, azimuth ramp, range ramp). We quantify the model fit using the Root Mean Square Error $\text{RMSE} = \sqrt{(\boldsymbol{d}_{obs} - \boldsymbol{d}_{sim})^T (\boldsymbol{d}_{obs} - \boldsymbol{d}_{sim})/n}$, with n is the number of samples.

For the afterslip models we solve the nonlinear inversion problem using a Sequential Monte Carlo sampling algorithm implemented in the Bayesian Earthquake Analysis Tool software (Vasyura-Bathke et al., 2019). For the viscoelastic relaxation model we use a grid search approach with the thickness of the upper accretionary prism (H) ranging from 4 to 14 km and the viscosity of the lower accretionary prism (η) ranging from 1×10^{15} Pa · s to 1×10^{21} Pa · s. The step sizes for H and $log(\eta)$ are 2 km and 0.25, respectively.

5. Results

5.1. Time Period 1

5.1.1. Viscoelastic Relaxation Models

The best-fitting model is found for a viscoelastic layer starting at 14 km depth. The spatial displacement pattern for the best-fitting model for power law rheology with $n = 3.5$ in the lower accretionary prism (H = 14 km, $\eta = 10^{18.75}$ Pa · s, Figure S3.1a in Supporting Information S1) does not explain the observations (Figure 2b). Linear Maxwell rheology and power law rheology with $n = 2$ in the lower prism do not provide any better fit (see Figure S3.3 in Supporting Information S1).

5.1.2. Aseismic Slip Models

Figures 2c–2f show that for all three model configurations there are fault geometries that explain the observed displacements equally well. The parameters for the best-fitting models are shown in Tables S2.1 to S2.4 of Supporting Information S1. For the best-fitting basal decollement model, the seven decollement dislocations have average width, dip, rake, slip and slip area of 31.0 km, 6°, 19°, 47 cm and 6,000 km² respectively, and the average rake and slip of coseismic dislocations are 28° and 10 cm (Figure 2e and Figure S4.2 days in Supporting
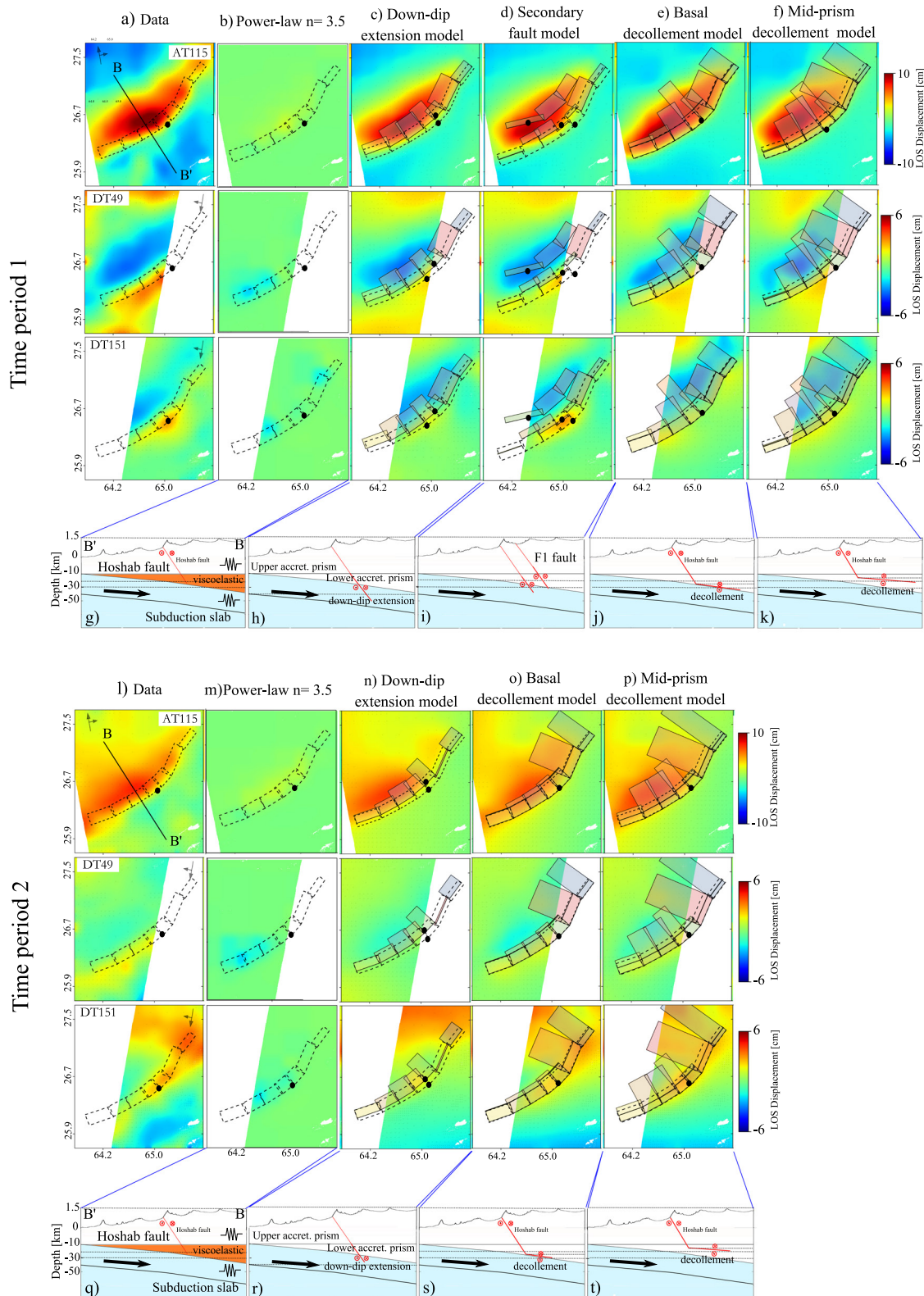
Figure 2.

Information S1, Table S2.3 in Supporting Information S1). For the best-fitting mid-prism decollement model, the seven decollement dislocations have average width, dip, rake, slip and slip area of 47.7 km, 7°, 22°, 25 cm and 11,000 km², respectively, and the average rake and slip of coseismic dislocations are 10° and 2 cm (Figure 2f and Figure S4.2e in Supporting Information S1, Table S2.4 in Supporting Information S1). Therefore, for the decollement models, most of the aseismic slip occurred on the decollement with little afterslip along the coseismic dislocations. The average ratio between the strike slip and dip slip, the equivalent moment released in percentage of the coseismic rupture, and the RMSE are about 3.3, 3.0, 2.9 and 2.5, 28%, 27%, 29% and 24%, and 0.015 m, 0.014 m, 0.015 m and 0.014 m for the down-dip extension, secondary fault, basal decollement and mid-prism decollement models, respectively.

5.2. Time Period 2

5.2.1. Viscoelastic Relaxation Models

Similar to time period 1, the best-fitting viscoelastic relaxation model with $n = 3.5$ power law rheology does not explain the observations (Figure 2m), nor does $n = 2$ or linear Maxwell rheology (see Figures S3.2 and S3.4 in Supporting Information S1). We conclude that the post-seismic displacements during this time period are also not due to viscoelastic relaxation.

5.2.2. Aseismic Slip Models

We test whether the down-dip extension model and the decollement models can explain the observed displacements. We find that for both models there are fault configurations that explain the data (Figures 2n–2p, see Tables S3.1 to S3.3 in Supporting Information S1). As time period 1, most of the aseismic slip occurred on the decollement faults with a little afterslip occurred on the coseismic dislocations for the decollement models. The average ratio between strike slip and dip slip, the moment released in percentage of the coseismic rupture, and the RMS are about 2.0, 1.4 and 1.3, 10.5%, 12.5% and 12.9% and 0.012 m, 0.011 m and 0.010 m for down-dip extension, basal decollement models and mid-prism decollement, respectively.

6. Coulomb Stress Change Modeling

As we cannot distinguish between the three aseismic slip models using the data misfit, we investigate whether afterslip and/or aseismic slip is consistent with stress changes due to the mainshock. For that we calculate the change in Coulomb failure stress $\Delta CFS = \Delta\tau + \mu'\Delta\sigma_n$ imparted by the main shock in the inferred direction of slip along the inferred fault planes of aseismic slip (Toda et al., 2011) in an elastic model (Poisson's ratio of 0.25 and Young's modulus of 30 GPa). Here $\Delta\tau$ is the change in shear stress, $\Delta\sigma_n$ the change in normal stress. For the coefficient of effective friction, μ', we use 0.2 because of the likely elevated fluid pressure. We use the earthquake slip distribution of Avouac et al. (2014). To increase the spatial resolution of stress changes we divide each fault segment into 5×5 or 5×2 patches.

Figure 3 shows that for the down-dip extension model and for the secondary fault model 86% and 66% of the fault patches received positive ΔCFS, whereas for the decollement models all fault patches received positive ΔCFS, with average ΔCFS of 0.25 and 0.22 MPa for the basal and mid-prism decollement models, respectively. Positive ΔCFS means that the mainshock encouraged the observed aseismic slip. Assuming that aseismic slip was driven by the mainshock-induced stress changes (in contrast to the regional stress field), this favors the decollement models. For $\mu' = 0.0$ representing lithostatic pore-fluid pressure, we obtained nearly identical results (Figure S7.1 in Supporting Information S1).

A comparison between the directions of aseismic slip for each fault segment with the directions of the maximum coseismic shear stress change (Figures 3e–3f, Figures S7.3–S7.4 in Supporting Information S1), shows that for both models they are very similar, and that the fault slipped in the direction of the imparted shear stress. The angle

Figure 2. (a) Interpolated observed line-of-sight (LOS) displacements of time period 1. Modeled LOS displacements of time period 1 for (b) viscoelastic relaxation model, (c) down-dip extension model, (d) secondary fault model, (e) basal decollement model and (f) mid-prism decollement model. In (a–f): Black dashed rectangle: coseismic fault segments; black dot: upper edge of the fault; black solid rectangle: aseismic slip faults. Conceptual sketches along profile BB' for (g) relaxation model, (h) down-dip extension model, (i) secondary fault model (j) basal decollement model and (k) mid-prism decollement model. Red dots: fault slip out of screen; red cross: fault slip into screen. For the original downsampled data see Figure S4.1 in Supporting Information S1 (l–t) same as (a–k) but for time period 2 and without secondary fault model.
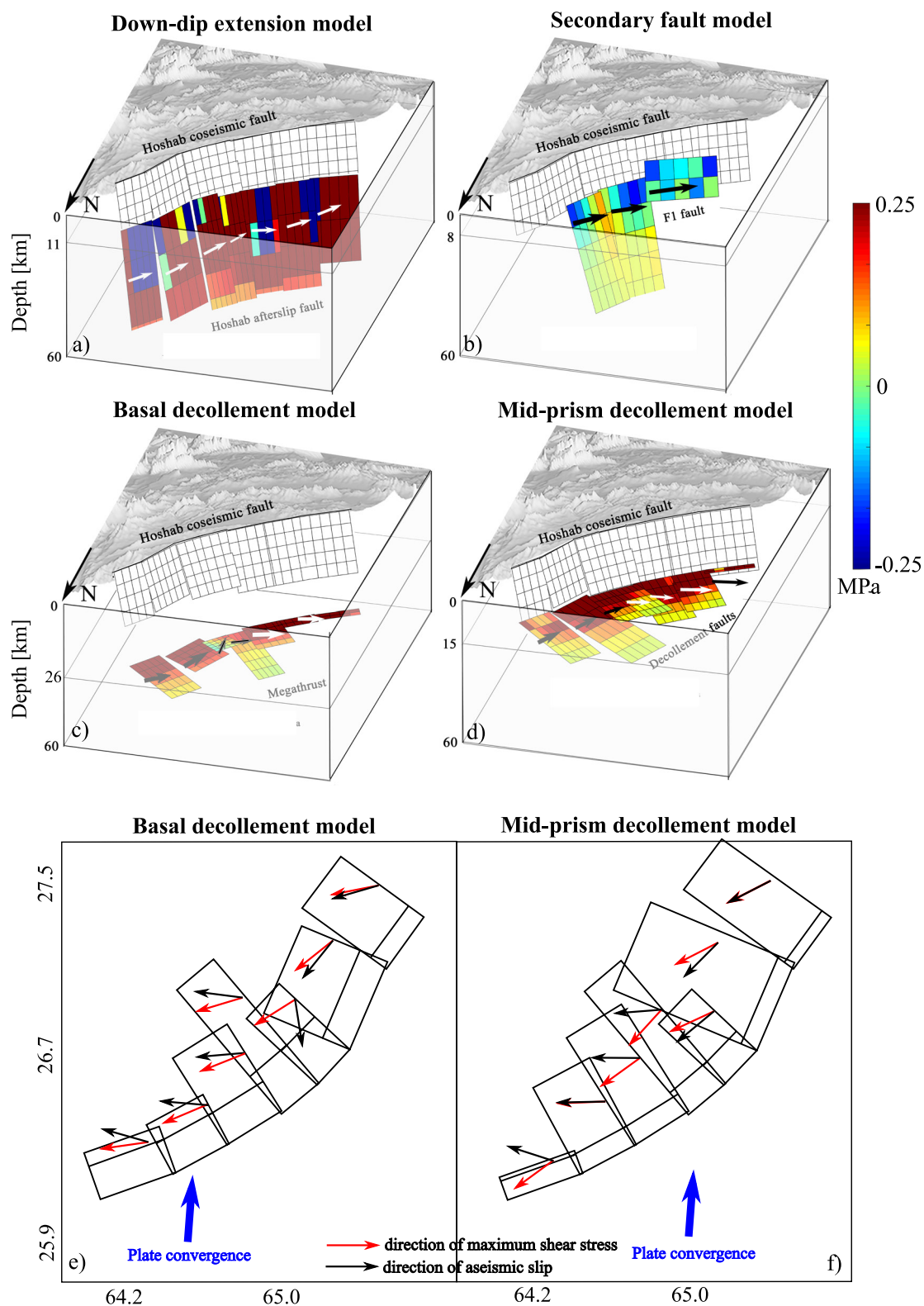
Figure 3.

between aseismic slip and plate convergence ranges from 120° to nearly 90° in the northeast and southwest of the aseismic slip area, respectively.

7. Discussion

7.1. No Viscoelastic Relaxation

The modeling shows that the observed post-seismic displacements can't be explained by viscoelastic relaxation. Our result of a fully elastic prism is consistent with the low heat flow and a strength-profile predicting elastic behavior to ∼40 km depth (see Figure S6 in Supporting Information S1), but not with a previous study which found viscoelastic relaxation for the lower prism (Peterson et al., 2018). The Figure S3.7 in Supporting Information S1 demonstrates that the Peterson et al. (2018) model does not explain the observations.

We also investigated whether viscoelastic relaxation in the upper mantle of the subducted slab could explain the observations but found that surface displacements are negligible (see Figure S3.5 in Supporting Information S1).

7.2. Aseismic Slip Along the Megathrust

We found that the post-seismic displacements are equally well explained by left-lateral slip along a slightly northwestward dipping decollement faults located at the base or in the interior of the accretionary prism at depths of 26 and 15 km, respectively. The trade-off between the depth and magnitude of slip along subhorizontal faults is a common limitation in geodetic inversions (e.g., Varugu & Amelung, 2021). The United States Geological Survey earthquake catalog shows only two Mw 4 aftershocks northwest of the Hoshab Fault, so we can exclude that the post-seismic displacements were caused by aftershocks.

Whatever its depth, the decollement is part of the Makran megathrust. Decollement faults can develop at different levels aided by elevated pore-fluid pressure (Ruh, 2017), for example, above areas of basal accretion by underplating. Intra-prism decollements are particularly common in prisms with high sedimentary input such as Makran (Kopp et al., 2000; Platt et al., 1985).

The megathrust moved an average of ∼80 cm, largely in direction of the maximum imparted shear stress (magnitude of 0.2–0.3 MPa). This agreement in direction is additional evidence that the slip occurred in response to the stress change imparted by the mainshock, and in particular by its left-lateral, strike-slip component. About 65%–96% (from northeast to southwest) of the aseismic slip occurred in direction perpendicular to the plate convergence direction, suggesting that there are only few, if at all, stresses due to plate loading.

The inferred aseismic slip implies low to zero plate coupling and velocity-strengthening frictional behavior for this section of the megathrust. Laboratory experiments have shown that high pore-fluid pressure causes velocity-strengthening frictional behavior (Xing et al., 2019).

Triggered aseismic slip in response to mainshock-induced stress changes has also been observed following the 1989 Loma Prieta earthquake (Lienkaemper et al., 1997) and the 2019 Ridgecrest earthquake (Barnhart et al., 2019).

7.3. Implications for the Seismic Potential of the Megathrust

The observation of aseismic slip along the megathrust under the inner Makran has implications for the maximum earthquake the subduction zone is able to generate. The 350–450°C isotherm which is considered as the down-dip limit of the seismogenic zone of megathrust faults (Bilek & Lay, 2018; Hyndman & Wang, 1993) occurs in the eastern Makran according to thermal models at 35 km depth (Khaledzadeh & Ghods, 2021; Smith et al., 2013) at 280 km distance from the trench. The seismic potential of the megathrust depends on the coupling between the

Figure 3. Coulomb stress changes in the direction of inferred slip along the aseismically sliping faults imparted by the coseismic slip distribution: (a) down-dip extension model; (b) F1 fault, (c) basal decollement model, (d) mid-prism decollement model. Black and white arrows: slip direction of the overriding block along the decollement. Direction of maximum coseismic shear stress and aseismic slip for (e) basal decollement model, (f) mid-prism decollement model, using unit length for arrows. Only coseismic faults from surface to 15 km depth are plotted considering that most coseismic slip occurred above 15 km depth (Avouac et al., 2014). The percentage of fault patches that received positive stress change are 137/160 = 86%, 40/60 = 66%, 145/145 = 100% and 160/160 = 100% (total number of fault patches in denominator) for the four models, respectively.
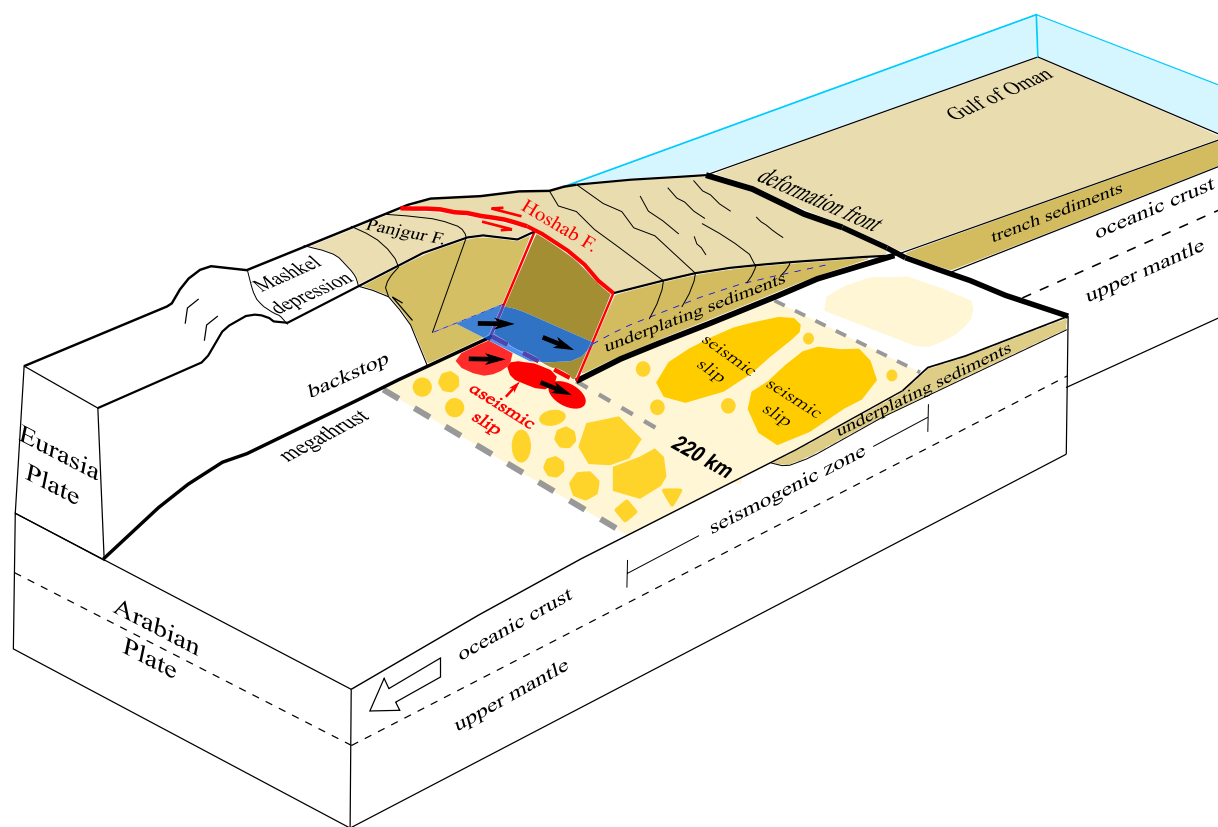
Figure 4. Schematic illustration of triggered aseismic slip (red patch) along the Makran megathrust. Blue patch and blue dashed line: alternate location of aseismic slip along mid-prism decollement fault above underplating sediments. Orange regions on megathrust: area of seismic slip; yellow regions: conditionally stable; white regions: aseismic slip.

overriding and the underthrusting plates. Sections of the fault can be fully locked (not slipping), partially coupled (slipping at rate lower than the plate convergence velocity) or fully decoupled (aseismic slip at plate convergence velocity) (Avouac, 2015). Our observation of aseismic slip at 220 km distance from the trench suggests that at this distance from the trench the megathrust is fully decoupled (Figure 4). This is roughly consistent with the plate coupling of 0.2–0.3 inferred by Lin et al. (2015) for this distance from the trench. The moment of a megathrust rupture from 60 to 220 km distance is ~25% less than the rupture considered by Smith et al. (2013). We highlight that this is an upper limit because our data don't constrain the coupling south of the Hoshab Fault. Throughout this paper we convert megathrust depth to distance from the trench using the slab geometry of Khaledzadeh and Ghods (2021).

8. Conclusions

We study the post-seismic displacement field starting 14 months after the 2013 Mw 7.7 Balochistan earthquake using Sentinel-1 InSAR time series data through April 2021. We show that the post-seismic displacements are due to aseismic slip along the megathrust northwest of the Hoschab fault. Triggered aseismic slip suggests that this segment of the megathrust is either partially or fully decoupled. The Eastern Makran megathrust appears to be locked to at most 220 km distance from the trench. A possible explanation for decoupling of this section of the megathrust are the particularly high pore fluid pressures typical for accretionary prisms in subduction zones with high sedimentary input.

Data Availability Statement

Sentinel-1 data are freely available from https://search.asf.alaska.edu/#/. The InSAR data are available from zenodo-https://zenodo.org/record/6233253#.YhXWTC-KGfV.

References

Avouac, J.-P. (2015). From geodetic imaging of seismic and aseismic fault slip to dynamic modeling of the seismic cycle. *Annual Review of Earth and Planetary Sciences*, *43*(1), 233–271. https://doi.org/10.1146/annurev-earth-060614-105302

Avouac, J.-P., Ayoub, F., Wei, S., Ampuero, J.-P., Meng, L., Leprince, S., et al. (2014). The 2013, Mw 7.7 Balochistan earthquake, energetic strike-slip reactivation of a thrust fault. *Earth and Planetary Science Letters*, *391*, 128–134. https://doi.org/10.1016/j.epsl.2014.01.036

Bagnardi, M., & Hooper, A. (2018). Inversion of surface deformation data for rapid estimates of source parameters and uncertainties: A Bayesian approach. *Geochemistry, Geophysics, Geosystems*, *19*(7), 2194–2211. https://doi.org/10.1029/2018GC007585

Barbot, S., & Fialko, Y. (2010a). Fourier-domain Green's function for an elastic semi-infinite solid under gravity, with applications to earthquake and volcano deformation. *Geophysical Journal International*, *182*(2), 568–582. https://doi.org/10.1111/j.1365-246X.2010.04655.x

Barbot, S., & Fialko, Y. (2010b). A unified continuum representation of post-seismic relaxation mechanisms: Semi-analytic models of afterslip, poroelastic rebound and viscoelastic flow. *Geophysical Journal International*, *182*(3), 1124–1140. https://doi.org/10.1111/j.1365-246X.2010.04678.x

Barnhart, W., Hayes, G., & Gold, R. (2019). The July 2019 Ridgecrest, California earthquake sequence: Kinematics of slip and stressing in cross-fault ruptures. *Geophysical Research Letters*, *46*, 11859–11867. https://doi.org/10.1029/2019GL084741

Barnhart, W. D., Hayes, G. P., Briggs, R. W., Gold, R. D., & Bilham, R. (2014). Ball-and-socket tectonic rotation during the 2013 Mw7.7 Balochistan earthquake. *Earth and Planetary Science Letters*, *403*, 210–216. https://doi.org/10.1016/j.epsl.2014.07.001

Bilek, S. L., & Lay, T. (2018). Subduction zone megathrust earthquakes. *Geosphere*, *14*(4), 1468–1500. https://doi.org/10.1130/ges01608.1

Burg, J.-P. (2018). Geology of the onshore Makran accretionary wedge: Synthesis and tectonic interpretation. *Earth-Science Reviews*, *185*, 1210–1231. https://doi.org/10.1016/j.earscirev.2018.09.011

Byrne, D. E., Sykes, L. R., & Davis, D. M. (1992). Great thrust earthquakes and aseismic slip along the plate boundary of the Makran Subduction Zone. *Journal of Geophysical Research*, *97*(B1), 449–478. https://doi.org/10.1029/91JB02165

Ellouz-Zimmermann, N., Deville, E., Müller, C., Lallemant, S., Subhani, A. B., & Tabreez, A. R. (2007). Impact of sedimentation on convergent margin tectonics: Example of the Makran accretionary prism (Pakistan). In *Thrust belts and foreland basins* (pp. 327–350). Heidelberg. https://doi.org/10.1007/978-3-540-69426-7_17

Fattahi, H., & Amelung, F. (2015). InSAR bias and uncertainty due to the systematic and stochastic tropospheric delay. *Journal of Geophysical Research: Solid Earth*, *120*, 8758–8773. https://doi.org/10.1002/2015JB012419

Fattahi, H., & Amelung, F. (2016). InSAR observations of strain accumulation and fault creep along the Chaman Fault system, Pakistan and Afghanistan. *Geophysical Research Letters*, *43*(16), 8399–8406. https://doi.org/10.1002/2016GL070121

Fattahi, H., Amelung, F., Chaussard, E., & Wdowinski, S. (2015). Coseismic and postseismic deformation due to the 2007 M 5.5 Ghazaband fault earthquake, Balochistan, Pakistan. *Geophysical Research Letters*, *42*, 3305–3312. https://doi.org/10.1002/2015GL063686

Fattahi, H., Simons, M., & Agram, P. (2017). InSAR time-series estimation of the ionospheric phase delay: An extension of the split range-spectrum technique. *IEEE Transactions on Geoscience and Remote Sensing*, *55*(10), 5984–5996. https://doi.org/10.1109/TGRS.2017.2718566

Frohling, E., & Szeliga, W. (2016). GPS constraints on interplate locking within the Makran subduction zone. *Geophysical Journal International*, *205*(1), 67–76. https://doi.org/10.1093/gji/ggw001

Gabi, L., Guy, M., Zhitu, M., & Mike, P. (2013). Update on CRUST1.0—A 1-degree global model of Earth's crust. *EGU; Geophysical Research Abstracts*, *15*.

Gavin, P. H., Ginevra, L. M., Daniel, E. P., Mike, H., Hanna, F., Maria, F., et al. (2018). Slab2, a comprehensive subduction zone geometry model. *Science*, *362*(6410), 58–61. https://doi.org/10.1126/science.aat4723

Hyndman, R. D., & Wang, K. (1993). Thermal constraints on the zone of major thrust earthquake failure: The Cascadia Subduction Zone. *Journal of Geophysical Research*, *98*(B2), 2039–2060. https://doi.org/10.1029/92JB02279

Jolivet, R., Duputel, Z., Riel, B., Simons, M., Rivera, L., Minson, S. E., et al. (2014). The 2013 Mw 7.7 Balochistan earthquake: Seismic potential of an Accretionary Wedge. *Bulletin of the Seismological Society of America*, *104*(2), 1020–1030. https://doi.org/10.1785/0120130313

Khaledzadeh, M., & Ghods, A. (2021). Estimation of size of megathrust zone in the Makran subduction system by thermal modelling. *Geophysical Journal International*, *228*(3), 1530–1540. https://doi.org/10.1093/gji/ggab417

Khan, M. A., & Raza, H. A. (1986). The role of geothermal gradients in hydrocarbon exploration in Pakistan. *Journal of Petroleum Geology*, *9*(3), 245–258. https://doi.org/10.1111/j.1747-5457.1986.tb00388.x

Kopp, C., Fruehn, J., Flueh, E. R., Reichert, C., Kukowski, N., Bialas, J., et al. (2000). Structure of the Makran subduction zone from wide-angle and reflection seismic data. *Tectonophysics*, *329*(1), 171–191. https://doi.org/10.1016/S0040-1951(00)00195-5

Lienkaemper, J. J., Galehouse, J. S., & Simpson, R. W. (1997). Creep response of the Hayward fault to stress changes caused by the Loma Prieta earthquake. *Science*, *276*(5321), 2014–2016. https://doi.org/10.1126/science.276.5321.2014

Lin, Y. n., Jolivet, R., Simons, M., Agram, P. S., Martens, H., Li, Z., et al. (2015). High interseismic coupling in the Eastern Makran (Pakistan) subduction zone. *Earth and Planetary Science Letters*, *420*, 116–126. https://doi.org/10.1016/j.epsl.2015.03.037

Lohdi, H., Ahmed, S., & Hasan, H. (2021). Tsunami heights and limits in 1945 along the Makran coast estimated from testimony gathered seven decades later in Gwadar, Pasni and Ormara. *Natural Hazards and Earth System Sciences*, *21*, 3085–3096. https://doi.org/10.5194/nhess-21-3085-2021

Mokhtari, M., Alaamjadi, A., Mahshadnia, L., & Rafizadeh, M. (2019). A review of the seismotectonics of the Makran Subduction Zone as a baseline for Tsunami Hazard Assessments. *Geoscience Letters*, *6*(1), 6–13. https://doi.org/10.1186/s40562-019-0143-1

Momeni, P., Goda, K., Heidarzadeh, M., & Qin, J. (2020). Stochastic analysis of tsunami hazard of the 1945 Makran subduction zone Mw 8.1–8.3 earthquakes. *Geosciences*, *10*(11), 452. https://doi.org/10.3390/geosciences10110452

Motaghi, K., Shabanian, E., & Nozad-Khalil, T. (2020). Deep structure of the western coast of the Makran subduction zone, SE Iran. *Tectonophysics*, *776*, 228314. https://doi.org/10.1016/j.tecto.2019.228314

Penney, C., Tavakoli, F., Saadat, A., Nankali, H. R., Sedighi, M., Khorrami, F., et al. (2017). Megathrust and accretionary wedge properties and behaviour in the Makran subduction zone. *Geophysical Journal International*, *209*(3), 1800–1830. https://doi.org/10.1093/gji/ggx126

Peterson, K. E., Barnhart, W. D., & Li, S. (2018). Viscous accretionary prisms: Viscoelastic relaxation of the Makran accretionary prism following the 2013 Baluchistan, Pakistan earthquake. *Journal of Geophysical Research: Solid Earth*, *123*(11), 10107–10123. https://doi.org/10.1029/2018JB016057

Pichon, X. L., & Kreemer, C. (2010). The Miocene-to-present kinematic evolution of the Eastern Mediterranean and Middle East and its implications for dynamics. *Annual Review of Earth and Planetary Sciences*, *38*(1), 323–351. https://doi.org/10.1146/annurev-earth-040809-152419

Platt, J. P., Leggett, J. K., Young, J., Raza, H., & Alam, S. (1985). Large-scale sediment underplating in the Makran accretionary prism. *Geology*, *13*(7), 507–511. https://doi.org/10.1130/0091-7613(1985)13<507:lsuitm>2.0.co;2

Rosen, P. A., Gurrola, E., Sacco, G. F., & Zebker, H. (2012). The InSAR scientific computing environment. In *EUSAR 2012; 9th European conference on synthetic aperture radar* (pp. 730–733). VDE. April 2012.

Ruh, J. (2017). Effect of fluid pressure distribution on the structural evolution of accretionary wedges. *Terra Nova*, *29*, 202–210. https://doi.org/10.1111/ter.12263

Smith, G., McNeill, L., Henstock, T. J., & Bull, J. (2012). The structure and fault activity of the Makran accretionary prism. *Journal of Geophysical Research*, *117*(B7). https://doi.org/10.1029/2012JB009312

Smith, G. L., McNeill, L. C., Wang, K., He, J., & Henstock, T. J. (2013). Thermal structure and megathrust seismogenic potential of the Makran subduction zone. *Geophysical Research Letters*, *40*(8), 1528–1533. https://doi.org/10.1002/grl.50374

Toda, S., Stein, R. S., Sevilgen, V., & Lin, J. (2011). *Coulomb 3.3 graphic-rich deformation and stress-change software for earthquake, tectonic, and volcano research and teaching - User guide* (p. 1060). U.S. Geological Survey Open-File Report.

Vallage, A., Klinger, Y., Grandin, R., Bhat, H. S., & Pierrot-Deseilligny, M. (2015). Inelastic surface deformation during the 2013 Mw 7.7 Balochistan, Pakistan, earthquake. *Geology*, *43*(12), 1079–1082. https://doi.org/10.1130/g37290.1

Varugu, B., & Amelung, F. (2021). Southward growth of Mauna Loa's dike-like magma body driven by topographic stress. *Scientific Reports*, *11*(1), 9816. https://doi.org/10.1038/s41598-021-89203-6

Vasyura-Bathke, H., Dettmer, J., Steinberg, A., Heimann, S., Isken, M. P., Zielke, O., et al. (2019). *BEAT: Bayesian Earthquake Analysis Tool*. GFZ Data Services. https://doi.org/10.5880/fidgeo.2019.024

Wang, R., Lorenzo-Martín, F., & Roth, F. (2006). PSGRN/PSCMP—A new code for calculating co- and post-seismic deformation, geoid and gravity changes based on the viscoelastic-gravitational dislocation theory. *Computers & Geosciences*, *32*(4), 527–541. https://doi.org/10.1016/j.cageo.2005.08.006

Xing, T., Zhu, W., French, M., & Belzer, B. (2019). Stabilizing effect of high pore fluid pressure on slip behaviors of gouge-bearing faults. *Journal of Geophysical Research: Solid Earth*, *124*(9), 9526–9545. https://doi.org/10.1029/2019JB018002

Yunjun, Z., Fattahi, H., & Amelung, F. (2019). Small baseline InSAR time series analysis: Unwrapping error correction and noise reduction. *Computers & Geosciences*, *133*, 104331. https://doi.org/10.1016/j.cageo.2019.104331

Zhou, Y., Elliott, J. R., Parsons, B., & Walker, R. T. (2015). The 2013 Balochistan earthquake: An extraordinary or completely ordinary event? *Geophysical Research Letters*, *42*(15), 6236–6243. https://doi.org/10.1002/2015GL065096

References From the Supporting Information

Doin, M. P., Lasserre, C., Peltzer, G., Cavalié, O., & Doubre, C. (2009). Corrections of stratified tropospheric delays in SAR interferometry: Validation with global atmospheric models. *Journal of Applied Geophysics*, *69*(1), 35–50. https://doi.org/10.1016/j.jappgeo.2009.03.010

Jolivet, R., Agram, P., Lin, Y. N., Simons, M., Doin, M. P., Peltzer, G., et al. (2014). Improving InSAR geodesy using Global Atmospheric Models. *Journal of Geophysical Research: Solid Earth*, *119*, 2324–2341. https://doi.org/10.1002/2013JB010588

Jolivet, R., Grandin, R., Lasserre, C., Doin, M. P., & Peltzer, G. (2011). Systematic InSAR atmospheric phase delay corrections from global meteorological reanalysis data. *Geophysical Research Letters*, *38*, L1731110. https://doi.org/10.1029/2011GL048757

Li, S., Moreno, M., Rosenau, M., Melnick, D., & Oncken, O. (2014). Splay fault triggering by great subduction earthquakes inferred from finite element models. *Geophysical Research Letters*, *41*(2), 385–391. https://doi.org/10.1002/2013GL058598

Stein, S., & Gordon, R. G. (1984). Statistical tests of additional plate boundaries from plate motion inversions. *Earth and Planetary Science Letters*, *69*(2), 401–412. https://doi.org/10.1016/0012-821X(84)90198-5